



Georeferencing Multi-source Geospatial Data Using Multi-temporal TerraSAR-X Imagery: a Case Study in Qixing Farm, Northeast China

QUANYING ZHAO, CHRISTOPH HÜTT, VICTORIA I. S. LENZ-WIEDEMANN, Cologne, YUXIN MIAO, Beijing, China, FEI YUAN, Mankato, MN, USA, FUSUO ZHANG, Beijing, China & GEORG BARETH, Cologne

Keywords: georeferencing, spatial inconsistency, multi-source data, TerraSAR-X, topographic vector data, optical remote sensing imagery

Summary: Geodata, including optical remote sensing (RS) images and topographic vector data, can be collected from multiple sources such as surveying and mapping agencies, commercial data acquisition companies, and local research institutes. These multi-source data have been widely used in past RS and geographic information system (GIS) studies in various applications. However, spatial inconsistencies inherent in the multi-source data require accurate georeferencing to be applied. This is challenging for study sites with limited accessibility and few reference maps. To address this challenge, this paper proposes an approach for generating ground control points (GCPs) using TerraSAR-X (TSX) data. In a case study, TSX images were used to georeference multi-source data covering the Qixing Farm in Northeast China. First, a stack of five multi-temporal TSX images were processed into one reference image to retrieve GCPs. These were then used to georeference the other datasets including Huanjing (HJ), Landsat 5 (LS 5), FORMOSAT-2 (FS-2), and RapidEye (RE) satellite images, as well as topographic vector datasets. Identifying tie points in the multi-source datasets and the corresponding GCPs in the TSX reference image enables georeferencing without field measurements. Finally the georeferencing accuracies for the optical RS images were assessed by using independent check points. Good results were obtained for the HJ, LS 5, FS-2 and RE images, with an absolute error of 7.15 m, 6.97 m, 8.94 m and 10.52 m, respectively. For the topographic vector datasets, ideal visual results were achieved, attributable to the rubber sheeting algorithm. These results demonstrate that the TSX reference image is suitable for georeferencing multi-source data accurately and cost-efficiently. The developed procedure can be applied in other study regions and is especially valuable for data-poor environments.

Zusammenfassung: Georeferenzierung von Raster- und Vektordaten aus unterschiedlichen Quellen mit Hilfe von multitemporalen TerraSAR-X-Aufnahmen – eine Fallstudie der Qixing-Farm im Nordosten Chinas. Für räumliche Analysen kommen Geodaten wie Fernerkundungsdaten und topographische Vektordaten zum Einsatz, die von diversen Einrichtungen, u.a. Vermessungsämtern, kommerziellen Geoinformations-Dienstleistern und Forschungsinstituten bereitgestellt bzw. bezogen werden. Diese aus unterschiedlichen Quellen stammenden Daten (Multidaten) werden für zahlreiche Anwendungen in Fernerkundungs- und GIS-Studien genutzt. Jedoch beinhalten diese Daten räumliche Ungenauigkeiten, die zunächst eine präzise Georeferenzierung erforderlich machen. Dieses stellt vor allem für Untersuchungsgebiete mit eingeschränkter Zugänglichkeit und nicht verfügbaren Referenzdaten eine Herausforderung dar. Dieser Artikel erklärt, wie Passpunkte aus Daten des Radarsatelliten TerraSAR-X (TSX) für die Georeferenzierung von Multidaten generiert werden können. In einer Fallstudie der Qixing-Farm im Nordosten Chinas wurden fünf multitemporale TSX-Radarbilder zu einem Referenzbild zusammengefügt, um mit hoher Genauigkeit Passpunkte abzuleiten. Diese Passpunkte dienen der Georeferenzierung mehrerer Multidaten aus diversen Quellen, welche sowohl Huanjing (HJ)-, Landsat 5 (LS 5)-, FORMOSAT-2 (FS-2)-, und RapidEye (RE)-Satellitenbilder als auch topographische Vektordaten umfassen. Die Identifizierung derselben Passpunkte in dem TSX-Referenzbild und in den Multidaten diverser Quellen ermöglicht eine genaue Georeferenzierung ohne im Gelände aufgenommene Messdaten. Die Genauigkeit der Georeferenzierung für die optischen Satellitenbilder wurde durch unabhängige Kontrollpunkte bewertet. Es wurden gute Ergebnisse für die HJ-, LS 5-, FS-2-

und RE-Satellitenbilder mit absoluten Fehlern von 7,15 m, 6,97 m, 8,94 m bzw. 10,52 m erzielt. Für die Georeferenzierung der topographischen Vektordaten wurden optimale visuelle Resultate erzielt, welches dem eingesetzten „Rubber Sheeting Algorithm“ zuzuschreiben ist. Diese Ergebnisse demonstrieren die Eignung der aus TSX-Daten abge-

leiteten Passpunkte, um Multidaten verschiedener Quellen genau und kosteneffizient zu georeferenzieren. Das entwickelte Verfahren kann auf andere Untersuchungsregionen übertragen werden und ist besonders wertvoll für Gegenden mit schlechter Verfügbarkeit von Referenzdaten.

1 Introduction

Data quality plays a critical role in geodata related research (BARETH 2009). To ensure data quality, georeferencing becomes a mandatory and crucial task. In this paper, datasets from different sources, each characterized by their unique attributes and properties, are referred to as multi-source data. Compared to single-source data, multi-source data can provide adequate information with different spatial and temporal resolutions, map scales, and spectral properties (LI 2010, WALDHOFF et al. 2012). Multi-source data provided by various governmental bureaus or non-governmental organizations such as local research institutions or special research groups may vary in many interpretation aspects and in terms of (spatial) data quality. Both geographic information system (GIS) and remote sensing (RS) data carry plenty of geospatial information but with different nature and content and with different semantics (WEIS et al. 2005). The integration of RS and GIS is emerging as a new research field (ZHANG 2010). GÓMEZ-CANDÓN et al. (2012) indicated that the locational errors in high resolution images, e.g. GeoEye-1 images, affect the delineation of the input prescription map which is a core problem for the implementation of site-specific agricultural management strategies. WEBER et al. (2008) confirmed that coregistration errors between imagery and field sites led to remarkable errors in landscape classification, particularly when the size of the target site was similar to the image pixel size. Moreover, in some cases, such as in China, detailed topographic data (1:5,000 – 1:25,000) with high spatial accuracy may not be accessible due to data sharing and management policies or lack of surveying and mapping activities (BARETH & YU 2004). Because of heterogeneous qualities, the integration and georeferencing processes for mul-

ti-source data are indispensable, complex and highly dependent on the purpose of the study.

A variety of methods for multi-source data integration and georeferencing have been developed in the past decades to eliminate spatial inconsistencies in multi-source datasets. For example, a Markov random field model was applied to merge images from multiple sensors for a land use classification (SOLBERG et al. 1996). A statistical approach to match relational features was introduced by WALTER & FRITSCH (1999). An iterative closest point algorithm was implemented to match features using a spatially precise map as the reference (VON GÖSSELN & SESTER 2004). Empirical and theoretical methods were implemented by USERY et al. (2009) for integrating the national maps of the United States with different scales and resolutions in vector and raster datasets. In addition, several automatic approaches have been developed to compute the imagery-to-vector conversion (WU et al. 2007), identify control point pairs from images using vector datasets as the glue layers (CHEN et al. 2006), conflate vector maps to high resolution imagery (SONG et al. 2009), or georeference image sequences in real-time (CHOI & LEE 2012).

In recent studies, Synthetic Aperture Radar (SAR) imagery has been used to quantify the spatial inconsistencies of geodata and to collect ground control points (GCPs) for georeferencing. SAR sensors are all-weather and day-night active microwave sensors that collect information of the targets according to the signal transport time between the sensor position and the terrain height. They have the potential to provide images with very high geometric accuracy (AGER & BRESNAHAN 2009, RODRÍGUEZ et al. 2006). In particular, the German TerraSAR-X (TSX) satellite launched in 2007 is equipped with a highly flexible phased

array antenna for SAR Stripmap, ScanSAR, and Spotlight operations (MITTERMAYER & RUNGE 2003). An overall ground accuracy of less than 1 m has been demonstrated when the images are projected to a precise terrain height (AGER & BRESNAHAN 2009, KOPPE et al. 2010, NONAKA et al. 2008). Therefore, the TSX products can be used to generate topographic maps and create accurate orthoimagery products (BADURSKA 2011, REINARTZ et al. 2011, SCHNEIDER et al. 2009).

To further explore the potential capability of TSX imagery as a source for locating GCPs and subsequently to georeference multi-source data characterized by varying properties and accuracies over a large area, a feasible and robust method which takes the advantage of the high spatial resolution and high geometric accuracy of TSX imagery is introduced. The main specific objectives are (i) to georeference topographic vector data from multiple sources; (ii) to improve the georeferencing results of Huanjing (HJ), Landsat 5 (LS 5), FORMOSAT-2 (FS-2), and RapidEye (RE) satellite images; and (iii) to assess the accuracy of georeferenced datasets and to evaluate if the results are highly dependent on the spatial accuracy of the TSX imagery.

2 Study Area and Data

2.1 Study Area

The Sanjiang Plain (SJP), located in Northeast China, is an alluvial plain formed by the Songhua River, the Heilong River and the Wusuli River. The topography is fairly flat with a slope of $< 0.012^\circ$. With an area of approximately 11 million ha, it is an important wetland area and ecosystem in China. Some wetland sites in this area have been designated for the list of wetlands of international importance (WANG et al. 2006). In addition, the SJP is the largest food base of China, where 52 national-owned farms are located. The climate is temperate sub-humid, with a mean annual precipitation of 500 mm – 600 mm (80% of it occurring between May and September), and an average temperature of 21°C – 22°C

in July and $\sim -18^\circ\text{C}$ in January. Nowadays, single season crops of paddy rice, soybean and maize are mainly planted in this area.

The study site Qixing Farm (47.2°N , 132.8°E), which covers an area of approximately 120,000 ha, is located in the central part of the SJP (Fig. 1). As of 2010, 62% of the study site was arable, dominated by three quarters of paddy rice and one quarter of dry-land (ZHANG 2012). In the paddy rice fields, rainfed and irrigation systems simultaneously exist. To improve the growing conditions of agricultural crops, shelter forests were planted in the late 1980s, primarily to reduce the speed of ground wind (LIU & ZHAO 1996).

2.2 Data Description

A time series of five TSX images (stripmap, VV-polarisation, incidence angle $\sim 35^\circ$, relative orbit 88, descending) was taken within 44 days from June 24 to August 7 of 2009 (see Tab. 1). These five stripmap images in the basic Single Look Slant Range Complex (SSC) form with intensity and phase information for each pixel in slant range geometry were used to create a TSX reference image. The orbit precision was set to ‘science’, which means that the satellite position during image acquisition is calculated with an error of less than 20 cm in a post processing step (FRITZ &

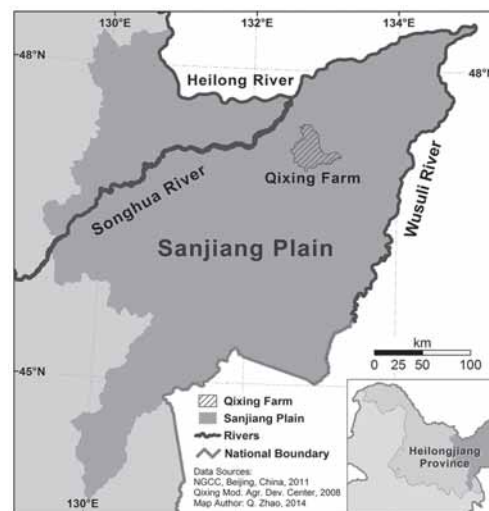


Fig. 1: Location of the study area Qixing Farm in Northeast China.

EINER 2013). This post processing dramatically increases the positional accuracy and thereby the image potential for generating GCPs (KOPPE et al. 2010).

The Qixing Farm field boundary file was produced by the Qixing Modern Agriculture Development Center. This GIS layer was given in Universal Transverse Mercator (UTM) coordinate reference system, zone 53 N. It provides the information on crop field boundaries, irrigation wells, water drainages, and shelter forests edges at a fine field unit scale. However, this dataset did not line up with any of the other datasets in our project. The inconsistency was nonsystematic in distance or directions (Fig. 3). An offset of more than 200 m between this dataset and the TSX images was identified in the northwest part, whereas in the southeast part the shift was more than 300 m in the opposite direction.

The public version of the 1:250,000 topographic vector dataset was produced by the National Geomatics Center of China (NGCC). This dataset includes multiple layers of administration boundaries, settlements, railways, roads, hydrological information, and landscapes. However, as BARETH & YU (2004) indicated, the spatial accuracy is not as high as expected. Therefore, a refined georeferencing of the public version is needed in this study.

The HJ, LS 5, FS-2, and RE satellite images were acquired from 2009 to 2012 in the growing season. The agricultural constructions, e.g. irrigation channels and raised ridges, for paddy rice in the study area are the same year

by year and the field boundaries are mostly stable. Therefore, one TSX reference image can be used in multiple years. The detailed information of the RS data is listed in Tab. 1.

3 Methods

3.1 Workflow of Georeferencing Multi-source Datasets

The schematic workflow of multi-source data georeferencing is shown in Fig. 2. There are mainly four steps involved: (1) pre-processing of the multi-temporal TSX images to generate one single reference image; (2) selection of GCPs from the processed TSX imagery and corresponding tie points from optical RS images or topographic vector maps; (3) reducing locational errors by recursively reselecting GCPs and corresponding tie points until achieving low positional error (PE) values or satisfactory visual results; (4) generating georeferenced datasets by image resampling or GIS data matching. Steps 1 and 2 are the key steps of this approach, which highly affect the quality of the GCP interpretation and consequently the final results.

We decided to use the PE because it is implemented in the software that we used and because the documentation of the individual error of every point proves best the efficiency of the proposed method. The standard deviation (Std.) that characterizes the overall error is also given as a comparison (Tab. 2).

Tab. 1: Characteristics of the RS images (az = azimuth, along track, rg = range, across track).

Satellite	Pixel Spacing (m)	Bands	Acquisition Date	Projection	Cloud Cover (%)	Processing Level
TSX	1.89 (az) × 1.57 (rg)	-	June 24, July 5, 16, 27, Aug. 7, 2009	WGS 84 UTM 53 N	--	SSC
HJ(CCD2)	30 × 30	4	June 29, 2012	WGS 84 UTM 53 N	0 (subset)	2
LS 5	30 × 30	7	Aug. 26, 2011	WGS 84 UTM 52 N	0 (subset)	1T
FS-2	2 × 2 (PAN)	5	July 6, 2009	Geographic (Lat/Lon)	0	1A
RE	5 × 5	5	May 19, 2012	WGS 84 UTM 53 N	0	3A

3.2 Creation of the Reference Image from TSX Stripmap Acquisitions

A stack of five TSX stripmap images was used to create the reference image. Radar image processing was performed using the Next ESA SAR Toolbox (NEST) distributed under the GNU General Public License. To meet the requirement of a geocoded image in which the precise outlines of objects are identifiable, certain pre-processing techniques were applied. First the ‘complex pixel value’ were used to calculate an amplitude image representing the strength of radar backscatter for each radar pixel cell. During the following

‘range Doppler terrain correctio’, the elevation data from the Space Shuttle Topography Mission (SRTM) in a spatial resolution of 3 arc-seconds served to transform the radar images from slant range geometry into the UTM coordinate reference system. Pixel spacing of the resultant geocoded product was set to 2 m to minimize spatial information loss, and to meet the file requirements of a manageable product. The main drawback of the SAR image with regard to the visible interpretation is the speckle effect which is an inherent noise of all radar images, often called grainy salt and pepper noise. To reduce this effect, a mean image of the five geocoded images was calculat-

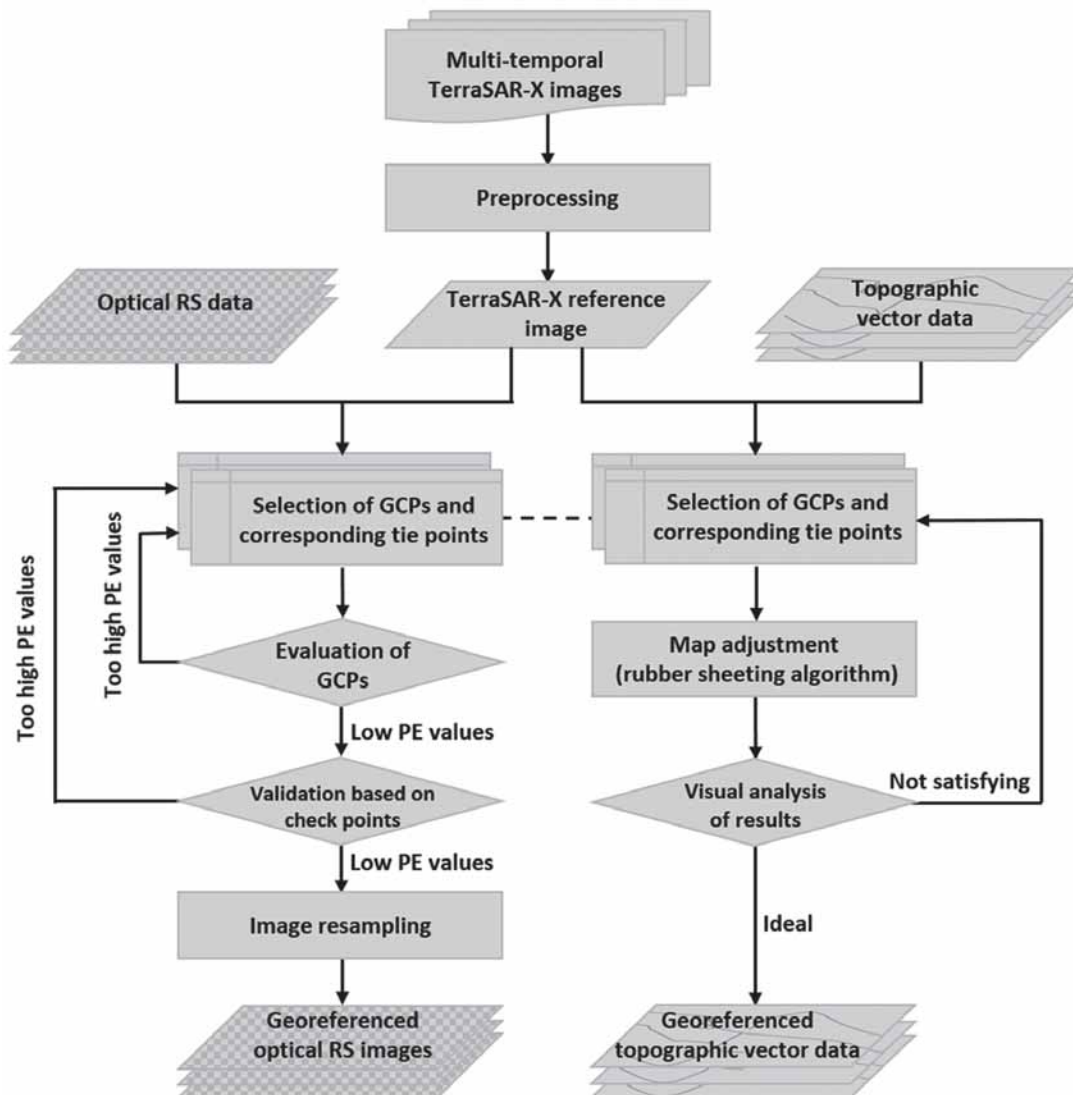


Fig. 2: Georeferencing workflow of the multi-source geospatial data, PE = positional error.

ed and a 3x3 mean speckle filter applied. The radiometric resolution was reduced from 16 bits to 8 bits. Therefore, the data size was considerably reduced. Likewise, the image representation speed was dramatically increased. In spite of a radiometric information loss during this procedure, the processed TSX reference image provides sufficient information for human interpreters to clearly define unambiguous GCPs with a high spatial resolution. Absolute radiometric calibration was not needed in this process as all five images have the same calibration constants, and moreover, the quantitative analysis of the backscattered signal was not the focus of this study. The resultant greyscale radar image was almost speckle-free and the shapes of all objects necessary in this research could be identified.

3.3 Georeferencing of Topographic Vector Data

Georeferencing of the topographic vector data was based on a rubber sheeting algorithm. The rubber sheeting, alternatively called rubber sheet, algorithm is one of the earliest and the most common computer cartogram algorithms (TOBLER 2004). This technique derives its name from the logical analogy of stretching a piece of rubber to fit over some objects (COBB et al. 1998). During the process, map areas are subdivided into triangular-shaped regions and local adjustments are applied on each single region. After that, each triangle either enlarges or shrinks iteratively toward its ideal size without changing the topology of the map (GILLMAN 1985, DOUGENIK et al. 1985). An iterative math-physical cartogram algorithm for continuous area was proposed by DOUGENIK et al. in 1985. This algorithm was recently improved by implementing an auxiliary quadtree structure in the process (SUN 2013a, 2013b).

In this study, the rubber sheeting tool of ArcGIS 10.1 was used to transfer the topographic vector data. Approximately 600 reference points, evenly distributed over the entire area of Qixing Farm, were selected as georeferencing points from the TSX reference image. As REINARTZ et al. (2009) proposed, the selection of reference points from the TSX image is not always a straightforward procedure. Based on

our experience, corresponding points were selected according to following rules: (i) Select points in the TSX reference image that are located at the intersection of the paddy field ridges, rural road edges, canopy crossings of different crops, or corners of artificial waters, which are in all cases clearly identifiable and unchanged during the 3 year-period from 2009 to 2012. (ii) Avoid elevated objects such as forest edges or tall buildings due to their systematic locational errors such as foreshortening, layover, and shadowing, induced by the radar imagery acquisition procedure. (iii) Select only points that have a corresponding (tie) point in the vector dataset, e.g. the Qixing Farm boundary data with line intersections and corners. A similar process was applied to the topographic GIS data provided by the NGCC.

3.4 Georeferencing of Optical RS Data

Multiple optical RS aforementioned data were also selected to demonstrate the georeferencing process based on the TSX reference image. In particular, image subsets covering the Qixing Farm were created for the HJ and LS 5 satellite data. All optical satellite images were georeferenced according to these main steps: First, all satellite images were reprojected into the UTM WGS 84 system to obtain an overview of the data inconsistencies. Second, a set of control points was selected from the TSX reference image based on the aforementioned rules. Consequently, the corresponding points have to match the objects which can be clearly identified in the optical RS imagery in this case. Third, in order to improve the transformation model and to minimize the errors caused by the manual measurement, GCPs and corresponding tie points were updated iteratively by eliminating the points with highest PEs and selecting additional control points until the residual errors fell below the maximum allowed value. The decision if a PE value was too high depended on the spatial resolution of the image to be georeferenced. For every single GCP, the maximum allowed value was within the subpixel range. Finally, a certain number of independent points were de-

fined as check points to evaluate the accuracy of the transformation. During the validation process, the GCPs were used to calculate the transformation model while the check points were used to evaluate the errors in the geometric transformation independently.

In our case, the PE is the horizontal distance between the input location of a GCP and the transformed location of the same GCP. The PE was calculated according to (CONGALTON & GREEN 2008).

$$PE = \sqrt{\Delta X^2 + \Delta Y^2} \quad (1)$$

where ΔX and ΔY are the positional differences between the reference point and the corresponding image or map position in the X and Y directions, respectively.

4 Results

4.1 Georeferencing Results of Topographic Vector Data

After the georeferencing based on the rubber sheeting algorithm, the georeferenced vector data of the Qixing Farm field boundaries (cyan) sufficiently fit to the new field boundaries which are clearly detectable in the TSX image. The problem of nonsystematic spatial inconsistency was well overcome and the shape of the vector graphics was preserved (Fig. 3). Similar results were also obtained for the topographic data provided by the NGCC.

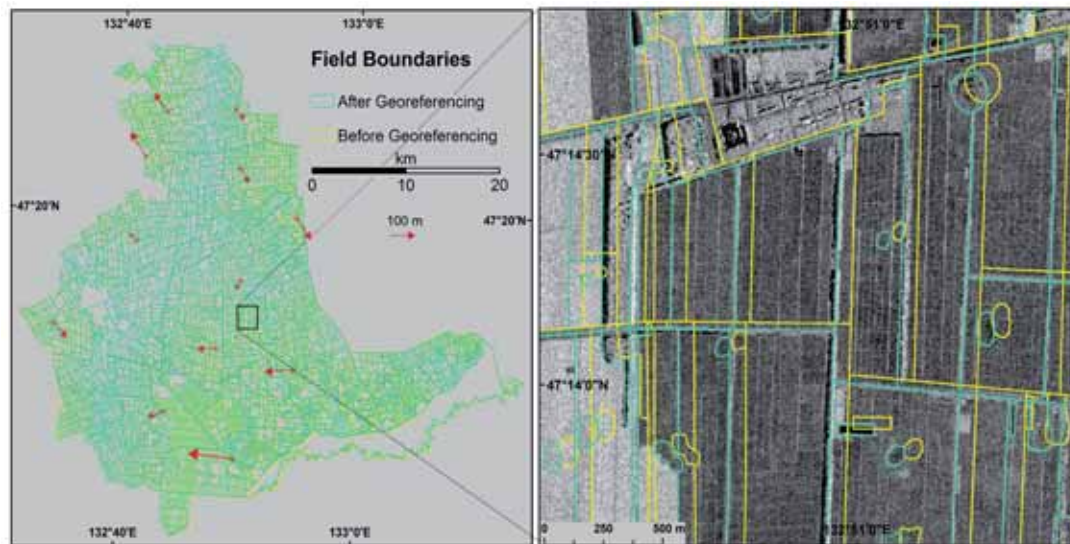


Fig. 3: Field boundary data, before (yellow) and after (cyan) the georeferencing; red arrows in the left figure show the vector force of the rubber sheeting procedure. Background data in the right figure: TSX reference image.

Tab. 2: Accuracy of the selected GCPs (PE = positional error, Std. = standard deviation).

Satellite	Pixel Size (resampled) (m)	Imagery/subset spatial extension (km)	Number of control points	PE (average) (m)	PE (max.) (m)	PE (min.) (m)	Std. (m)
HJ (CCD2)	30 × 30	55 × 55	100	12.66	27.39	1.87	6.70
LS 5	30 × 30	48 × 68	220	9.04	16.63	0.59	3.85
FS-2	2 × 2 (PAN)	30 × 28	143	3.43	5.91	0.3	1.35
RE	5 × 5	24 × 24	64	4.09	9.36	0.60	2.12

4.2 Georeferencing Results of Optical RS Data

Optical RS data were georeferenced according to the method described in the previous sections. Tab.2 shows the relevant information of the selected GCPs.

After recursively selecting control points, the final PEs were less than half a pixel for both the HJ (CCD2) and LS 5 images, and nearly one pixel for the FS-2 and RE images. Fig. 4 shows the georeferencing results visually. The ground features from each of the images fit well. The roads match properly in all

images and the paddy field block boundaries are ideally aligned to each other in the higher resolution images (TSX, FS-2 and RE).

4.3 Spatial Accuracies of the Georeferenced Optical RS Data

To evaluate the spatial accuracies of the georeferenced optical RS data, independent check points covering the whole scene were created and their spatial parameters were analyzed. To capture the maximum PE results, the check points were located in the areas where the

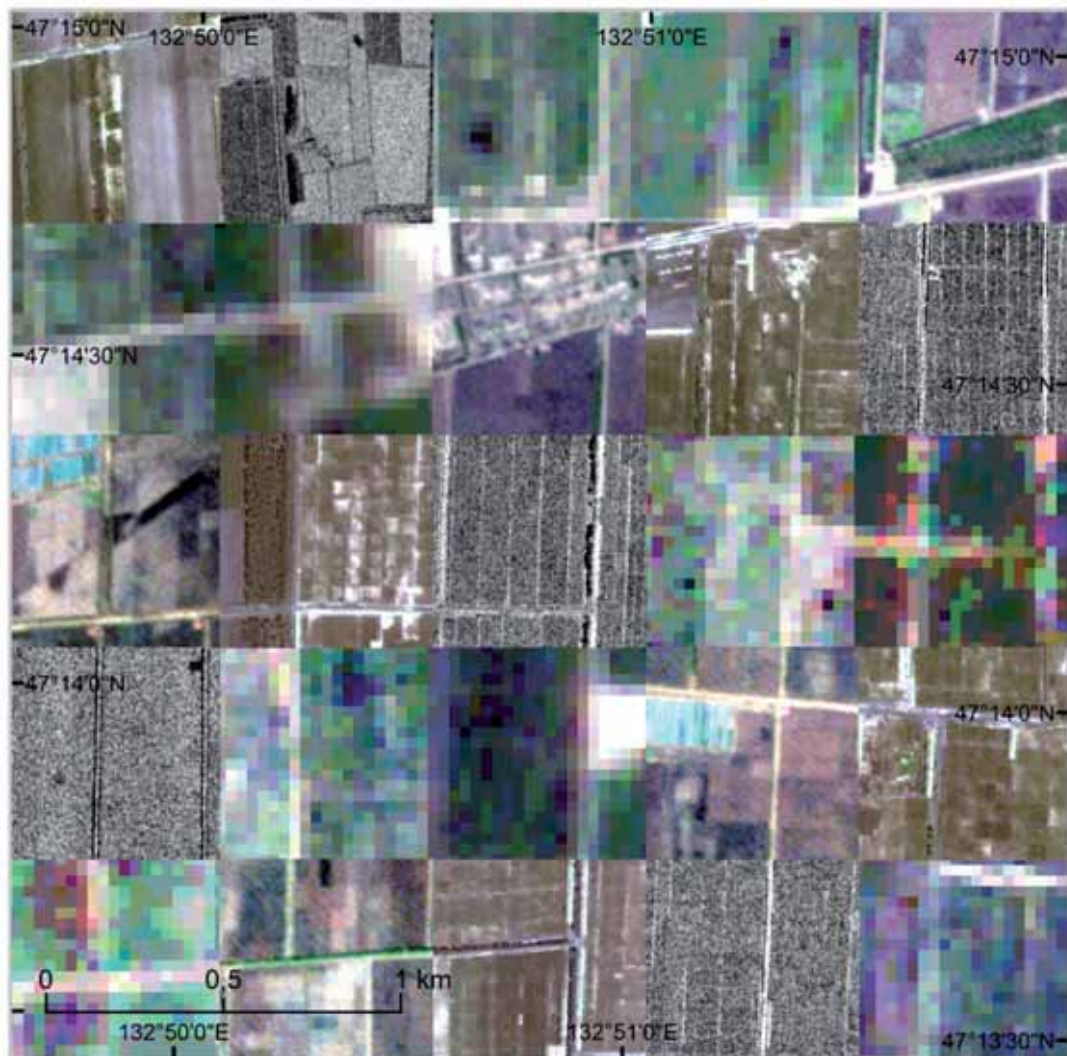


Fig. 4: An example of georeferenced multi-source RS images in comparison to the TSX image. From left to right: 1st row: FS-2, TSX, LS 5, HJ, RE; 2nd row: LS 5, HJ, RE, FS-2, TSX; 3rd row: RE, FS-2, TSX, LS 5, HJ; 4th row: TSX, LS 5, HJ, RE, FS-2; 5th row: HJ, RE, FS-2, TSX, LS 5.

Tab. 3: Accuracy of the independent check points.

Satellite	Pixel Size (resampled) (m)	Imagery/ subset spatial extension (km)	Number of check points	PE (average) (m)	PE (max.) (m)	PE (min.) (m)	Std. (m)
HJ (CCD2)	30 × 30	55 × 55	20	3.29	8.05	1.81	1.55
LS 5	30 × 30	48 × 68	34	3.11	6.48	1.80	1.11
FS-2	2 × 2	30 × 28	30	5.08	7.44	1.07	1.89
RE	5 × 5	24 × 24	10	6.66	8.42	4.08	1.21

GCP density was relatively low. The results were summarized in Tab. 3. The average PEs of the check points were at a sub-pixel value (slightly more than 0.1 pixel) in the HJ (CCD2) and LS 5 images. Accuracies of 2.5 pixels and 1.3 pixels were achieved for the FS-2 and RE imagery, respectively. The average PE values for all four types of satellite images ranged from 3.11 m to 6.66 m.

5 Discussion

5.1 Analysis of the Anticipated Spatial Error in the Processed TSX Reference Image

The geometric distortion of SAR imagery products can be caused by three components (CURLANDER & McDONOUGH 1991): (i) sensor/platform instability and signal propagation effects, (ii) terrain height, and (iii) processor induced errors. The uncertainties embedded in the SSC products comprise only the first type of error, which is less than 1 m (NONAKA et al. 2008, FRITZ & EINEDER 2013). The second type of errors comes from the SRTM DEM dataset. RODRIGUEZ et al. (2006) found that the absolute height error of the SRTM in Eurasia was less than 6.2 m; whereas in the SJP study site, where the topography is fairly flat, the absolute error was less than 2 m according to the SRTM THED (terrain height error data) product.

Hence, the target range location error (ΔR) determined by the terrain height estimation can be calculated using (2) (CURLANDER & McDONOUGH 1991):

$$\Delta R = \Delta h / \tan \eta, \quad (2)$$

where Δh is the height (DEM elevation) estimation error (2 m) and η is the location incidence angle (35° in this study). Therefore, the ΔR for this study was calculated as 2.86 m. The processor induced error is process dependent and is denoted as $\Delta \delta_i$. The overall absolute spatial error of the projected TSX imagery can therefore be calculated by these three components, with the result of $(3.86 + \Delta \delta_i)$ m. Where the processor induced error $\Delta \delta_i$ during TSX image processing can be assumed to be infinitely small.

5.2 Quantified Spatial Accuracy of the Georeferenced Datasets

Considering all spatial inconsistent sources, the overall absolute error of the georeferenced datasets can be estimated. The overall errors of the georeferenced optical RS data, which is equal to the sum of the PE in Tab. 3 and the geometric distortion of the TSX image (3.86 m), were 7.15 m, 6.97 m, 8.94 m, and 10.52 m for HJ, LS 5, FS-2, and RE satellite images, respectively. DAI & KHORRAM (1998) found that a registration error of less than one-fifth of a pixel should be achieved to detect 90% of the true changes. Hence, the registration results for the HJ (CCD2) and LS 5 images can support a change detection analysis with a spatial error close to 10%.

In surface area estimation, OZDOGAN & WOODCOCK (2006) noted that spatial errors are dependent on both RS image resolution and the field size because of ‘the distribution of subpixel proportions’, especially when the field size is similar to or less than the RS data resolution. In this study, the results of the FS-2 and RE images processing are suf-

ficient for field-unit level analysis since the size of each field block unit is typically larger than 5,000 m². The field block is the smallest area of a farm management unit and is considered as the primary scale for management decisions. The high accuracies for the HJ and LS 5 image processing are also beneficial for studies at the farmer-unit level, as a farmer's crop field is generally larger than 20 ha. Fig. 5 provides a visual result of datasets from multiple sources over the entire area of the Qixing Farm.

5.3 Feasibility of the Approach

In this study, topographic vector datasets and optical RS images from multiple sources were georeferenced using GCPs derived from the TSX reference image without the need for labour intensive field work. The creation of the TSX reference image and its use to locate accurate GCPs is critical, because it not only determines the precision of the results but also the feasibility of this method.

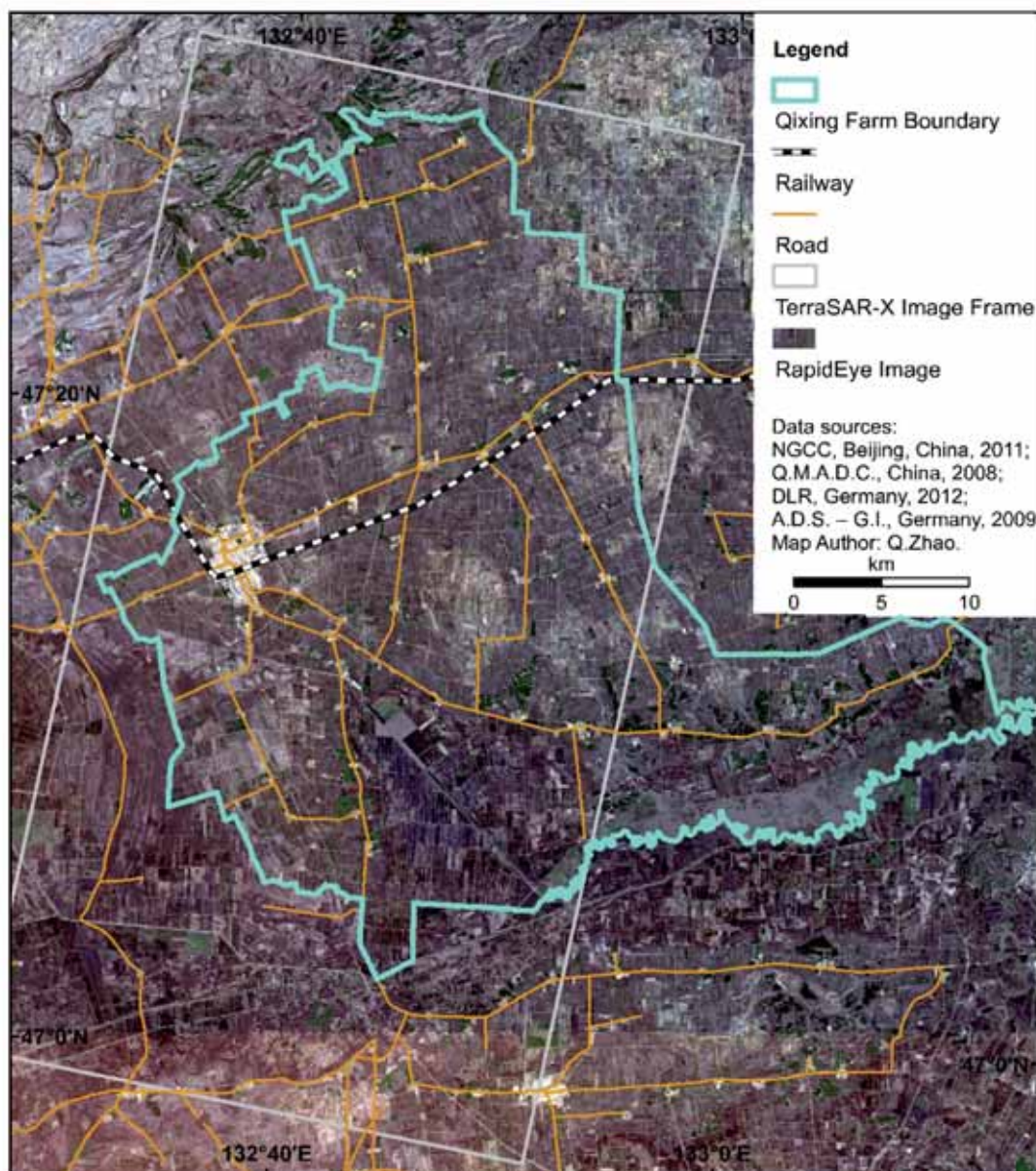


Fig. 5: Georeferenced multi-source data for the study area of Qixing Farm.

Although many studies (SOWMYA & TRINDER 2000, SOHN & DOWMAN 2007, REINARTZ et al. 2009) have attempted to extract geometric features, e.g. GCPs, automatically from satellite images, there is a lack of reports on automatic methods for georeferencing multi-source data. Automatic feature extraction methods have limited applicability due to their complex parameterization and strict condition requirements (COBB et al. 1998). Moreover, automatic methods for integrating GIS data and satellite imagery are rare.

The strategy proposed in this study showed that for each dataset, different GCPs were required due to the diverse characteristics of the multi-source data. Manual procedure meets this requirement and ensures the spatial accuracy. Although the high resolution TSX imagery supplies a sufficient number of GCPs, the selection of the GCPs and their corresponding tie points is never straightforward. There is still a need to establish the criteria for selecting reference points systematically. Another drawback of this method is its inefficiency in processing a large number of datasets. However, the proposed method still is especially valuable for data-poor environments lacking reference data.

6 Conclusions

This study provides an applicable and cost-effective approach for georeferencing multi-source data with different characteristics and non-systematic spatial inconsistencies. It is an especially beneficial technique for large study sites with limited accessibility and reference maps. The results demonstrated the feasibility of using TSX imagery to accurately georeference multi-source datasets without in-situ GCP data collection. By using the mean of five TSX images and the mean filter, a speckle-free reference image was generated. This proved to be critical for locating sufficient GCPs successfully. The PEs of the check points were less than 0.2 pixel for the 30 m resolution images (HJ and LS), approximately 2.5 pixels for the FS-2 images, and 1.3 pixels for the RE images. The overall errors were nearly less than 10 m for all four types of images. The discrepancies among each pair of the TSX and GIS

data were only assessed visually, which demonstrates a need for further study.

Acknowledgements

This research was funded by the Natural Science Foundation of China (NSFC, project No. 31071859), the International Bureau of the German Federal Ministry of Education and Research (BMBF, project No. 01DO12013), and the German Research Foundation (DFG, project No. BA 2062/8-1). The TerraSAR-X images were provided by the Airbus Defence and Space – Geo-Intelligence. The GIS data layer of the Qixing Farm field boundary was provided by the Qixing Modern Agriculture Development Center in Heilongjiang, China. The 1:250,000 scale topographic dataset with multiple layers for the study area was provided by the National Geomatics Center of China (NGCC) (<http://ngcc.sbsm.gov.cn/>). The Huanjing satellite images were acquired from the China Centre for Resources Satellite Data and Application (CCRSDA) (<http://www.cresda.com/n16/index.html>). The Landsat 5 TM images were downloaded from the website of the Earth Resources Observation and Science (EROS) Center of U.S. Geological Survey (USGS) (<http://eros.usgs.gov/>). The FORMOSAT-2 images were obtained from the National Space Organization (NSPO) of Taiwan. The RapidEye satellite images were kindly provided by the RE Science Archive (RESA), German Aerospace Center (Deutsches Zentrum für Luft- und Raumfahrt, DLR). The leading author would also like to acknowledge the support of the China Scholarship Council (Nov. 2010 – Oct. 2014), Beijing, China.

References

- AGER, T.P. & BRESNAHAN, P.C., 2009: Geometric precision in space radar imaging: results from TerraSAR-X. – ASPRS Annual Conference, Baltimore, MD, USA.
- BADURSKA, M., 2011: Orthorectification and Geometric Verification of High Resolution TerraSAR-X Images. – *Geomatics and Environmental Engineering* **5** (3): 13–25.

- BARETH, G. & YU, Z., 2004: Verfügbarkeit von digitalen Geodaten in China. – *Petermanns Geographische Mitteilungen* **148** (5): 78–85 (written in German with English abstract).
- BARETH, G., 2009: GIS- and RS-based spatial decision support: structure of a spatial environmental information system (SEIS). – *International Journal of Digital Earth* **2** (2): 134–154.
- CHEN, C.C., KNOBLOCK, C.A. & SHAHABI, C., 2006: Automatically conflating road vector data with orthoimagery. – *GeoInformatica* **10** (4): 495–530.
- CHOI, K. & LEE, I., 2012: A sequential aerial triangulation algorithm for real-time georeferencing of image sequences acquired by an airborne multi-sensor system. – *Remote Sensing* **5** (1): 57–82.
- COBB, M.A., CHUNG, M.J., FOLEY, H., PETRY, F.E. & SHAW, K.B., 1998: A Rule-based Approach for the Conflation of Attributed Vector Data. – *GeoInformatica* **2** (1): 7–35.
- CONGALTON, R.G. & GREEN, K., 2008: Assessing the accuracy of remotely sensed data: principles and practices. – 183 p., CRC press, Boca Raton, FL, USA.
- CURLANDER, J.C. & McDONOUGH, R.N., 1991: Synthetic aperture radar: systems and signal processing. – 1st edition, 672 p., Wiley, New York, NY, USA.
- DAI, X. & KHORRAM, S., 1998: The effects of image misregistration on the accuracy of remotely sensed change detection. – *IEEE Transactions on Geoscience and Remote Sensing* **36** (5): 1566–1577.
- DOUGENIK, J.A., CHRISMAN, N.R. & NIEMEYER, D.R., 1985: An algorithm to construct continuous area cartograms. – *The Professional Geographer* **37**: 75–81.
- FRITZ, T. & EINEDER, M., 2013 (eds.): TerraSAR-X Ground Segment. – Basic Product Specification Document. Issue 1.9, Doc.: TX-GS-DD-3302, DLR. https://tandemx-science.dlr.de/pdfs/TX-GS-DD-3302_Basic-Products-Specification-Document_V1.9.pdf (18.4.2014).
- GILLMAN, D.W., 1985: Triangulations for rubber-sheeting. – 7th International Symposium on Auto-Carto: 191–199, Washington D.C., USA.
- GÓMEZ-CANDÓN, D., LÓPEZ-GRANADOS, F., CABALLERO-NOVELLA, J.J., PEÑA-BARRAGÁN, J.M. & GARCÍA-TORRES, L., 2012: Understanding the errors in input prescription maps based on high spatial resolution remote sensing images. – *Precision Agriculture* **13** (5): 581–593.
- KOPPE, W., KIEFL, N., HENNIG, S. & JANOTH, J., 2010: Validation of Pixel Location Accuracy of Orthorectified TerraSAR-X Products. – 8th European Conference on Synthetic Aperture Radar (EU-SAR), Aachen.
- LI, D., 2010: Remotely sensed images and GIS data fusion for automatic change detection. – *International Journal of Image and Data Fusion* **1** (1): 99–108.
- LIU, T. & ZHAO, Y., 1996: Ecological benefit analysis and estimation of the forest shelter in the Nongken area, Sanjiang Plain. – *Forest Science and Technology* **5**: 12–14 (written in Chinese).
- MITTERMAYER, J. & RUNGE, H., 2003: Conceptual studies for exploiting the TerraSAR-X dual receive antenna. – IGARSS: 2140–2142, Toulouse, France.
- NONAKA, T., ISHIZUKA, Y., YAMANE, N., SHIBAYAMA, T., TAKAGISHI, S. & SASAGAWA, T., 2008: Evaluation of the geometric accuracy of TerraSAR-X. – *The International Archives of the Photogrammetry, Remote Sensing and Spatial Information Sciences XXXVII*, Beijing, China.
- OZDOGAN, M. & WOODCOCK, C.E., 2006: Resolution dependent errors in remote sensing of cultivated areas. – *Remote Sensing of Environment* **103** (2): 203–217.
- REINARTZ, P., MÜLLER, R., SURI, S., SCHNEIDER, M., SCHWIND, P. & BAMLER, R., 2009: Using geometric accuracy of TerraSAR-X data for improvement of direct sensor orientation and ortho-rectification of optical satellite data. – *IEEE International Geoscience & Remote Sensing, IGARSS 5*: V-44–V-47, Cape Town, South Africa.
- REINARTZ, P., MULLER, R., SCHWIND, P., SURI, S. & BAMLER, R., 2011: Orthorectification of VHR optical satellite data exploiting the geometric accuracy of TerraSAR-X data. – *ISPRS Journal of Photogrammetry and Remote Sensing* **66** (1): 124–132.
- RODRÍGUEZ, E., MORRIS, C.S. & BELZ, J.E., 2006: A Global Assessment of the SRTM Performance. – *Photogrammetric Engineering & Remote Sensing* **72** (3): 249–260.
- SCHNEIDER, M., MÜLLER, R., KRAUSS, T., REINARTZ, P., HÖRSCH, B. & SCHMUCK, S., 2009: Urban Atlas – DLR Processing Chain for Orthorectification of Prism and AVNIR-2 Images and TerraSAR-X as possible GCP Source. – 3rd ALOS PI Symposium: 1–6, Kona, HI, USA. http://www.asf.alaska.edu/content/pi_symp/Schneider_M._urban-paper.pdf (20.4.2014).
- SOHN, G. & DOWMAN, I., 2007: Data fusion of high-resolution satellite imagery and LiDAR data for automatic building extraction. – *ISPRS Journal of Photogrammetry and Remote Sensing* **62** (1): 43–63.
- SOLBERG, A.H.S., TAXT, T. & JAIN, A.K., 1996: A Markov random field model for classification of multisource satellite imagery. – *IEEE Transactions*

- tions on *Geoscience and Remote Sensing* **34** (1): 100–113.
- SONG, W., KELLER, J.M., HAITHCOAT, T.L. & DAVIS, C.H., 2009: Automated Geospatial Conflation of Vector Road Maps to High Resolution Imagery. – *IEEE Transactions on Image Processing* **18** (2): 388–400.
- SOWMYA, A. & TRINDER, J., 2000: Modelling and representation issues in automated feature extraction from aerial and satellite images. – *ISPRS Journal of Photogrammetry and Remote Sensing* **55** (1): 34–47.
- SUN, S., 2013a: An optimized rubber-sheet algorithm for continuous area cartograms. – *Professional Geographer* **65** (1): 16–30.
- SUN, S., 2013b: A fast, free-form rubber-sheet algorithm for contiguous area cartograms. – *International Journal of Geographical Information Science* **27** (3): 567–593.
- TOBLER, W., 2004: Thirty five years of computer cartograms. – *Annals of the Association of American Geographers* **94** (1): 58–73.
- USERY, E.L., FINN, M.P. & STARBUCK, M., 2009: Data layer integration for the national maps of the United States. – *Cartographic Perspectives* **62**: 28–41.
- VON GÖSSELN, G.V. & SESTER, M., 2004: Integration of geoscientific data sets and the German digital map using a matching approach. – XXth Congress of the International Society for Photogrammetry and Remote Sensing, Commission IV, XXXV-B4: 1247, Istanbul, Turkey.
- WALDHOFF, G., CURDT, C., HOFFMEISTER, D. & BARETH, G., 2012: Analysis of multitemporal and multisensor remote sensing data for crop rotation mapping. – XXIIth Congress of the International Society for Photogrammetry and Remote Sensing, Melbourne, Australia.
- WALTER, V. & FRITSCH, D., 1999: Matching spatial datasets: A statistical approach. – *International Journal of Geographical Information Science* **13** (5): 445–473.
- WANG, Z., ZHANG, B., ZHANG, S., LI, X., LIU, D., SONG, K., LI, J., LI, F. & DUAN, H., 2006: Changes of land use and of ecosystem service values in Sanjiang Plain, northeast China. – *Environmental Monitoring and Assessment* **112** (1–3): 69–91.
- WEBER, K.T., THÉAU, J. & SERR, K., 2008: Effect of coregistration error on patchy target detection using high-resolution imagery. – *Remote Sensing of Environment* **112** (3): 845–850.
- WEIS, M., MÜLLER, S., LIEDTKE, C.-E. & PAHL, M., 2005: A framework for GIS and imagery data fusion in support of cartographic updating. – *Information Fusion* **6** (4): 311–317.
- WU, X., CARCERONI, R., FANG, H. & KIRMSE, A., 2007: Automatic alignment of large-scale aerial rasters to road-maps. – 15th annual ACM international symposium on Advances in geographic information systems, Seattle, WA, USA.
- ZHANG, J., 2010: Multi-source remote sensing data fusion: status and trends. – *International Journal of Image and Data Fusion* **1** (1): 5–24.
- ZHANG, W., 2012: Personal communication, Qixing Farm, June 2012.

Addresses of the Authors:

M.SC. QUANYING ZHAO, Dipl.-Geogr. CHRISTOPH HÜTT, Dr. VICTORIA I.S. LENZ-WIEDEMANN & Prof. Dr. GEORG BARETH, International Center for Agro-Informatics and Sustainable Development (ICASD) (www.icasd.org), Institute of Geography, GIS & RS Group, University of Cologne, D-50923 Köln, Tel.: +49-221-470-1951, e-mail: zhaoquanying@gmail.com, {christoph.huett}{victoria.lenz}{g.bareth}@uni-koeln.de

Prof. Dr. YUXIN MIAO, ICASD, College of Resources and Environmental Sciences, China Agricultural University, Beijing China, 100193 Beijing, Tel.: +86-10-6273-2865, e-mail: ymiao@cau.edu.cn

Prof. Dr. FEI YUAN, ICASD, Department of Geography, Minnesota State University, Minnesota, MN 56001, USA, Tel.: +1-507-389-2376, e-mail: fei.yuan@mnsu.edu

Prof. Dr. FUSUO ZHANG, College of Resources and Environmental Sciences, China Agricultural University, Beijing China, 100193 Beijing, Tel.: +86-10-6273-2499, e-mail: zhangfs@cau.edu.cn

Manuskript eingereicht: August 2014

Angenommen: Dezember 2014